FITEE

Initial-condition-switched boosting extreme multistability and mechanism analysis in a memcapacitive oscillator[*]

Bei CHEN, Quan XU, Mo CHEN, Huagan WU, Bocheng BAO[†‡]

School of Microelectronics and Control Engineering, Changzhou University, Changzhou 213164, China

[†]E-mail: mervinbao@126.com

Abstract: Extreme multistability has seized scientists' attention due to its rich diversity of dynamical behaviors and great flexibility in engineering applications. In this paper, a four-dimensional (4D) memcapacitive oscillator is built using four linear circuit elements and one nonlinear charge-controlled memcapacitor with a cosine inverse memcapacitance. The 4D memcapacitive oscillator possesses a line equilibrium set, and its stability periodically evolves with the initial condition of the memcapacitor. The 4D memcapacitive oscillator exhibits initial-condition-switched boosting extreme multistability due to the periodically evolving stability. Complex dynamical behaviors of period doubling/halving bifurcations, chaos crisis, and initial-condition-switched coexisting attractors are revealed by bifurcation diagrams, Lyapunov exponents, and phase portraits. Thereafter, a reconstructed system is derived via integral transformation to reveal the forming mechanism of the initial-condition-switched boosting extreme multistability in the memcapacitive oscillator. Finally, an implementation circuit is designed for the reconstructed system, and Power SIMulation (PSIM) simulations are executed to confirm the validity of the numerical analysis.

1 Introduction

Memory effects are widespread in nature and become especially important at the nanoscale where the dynamics of electrons and ions strongly depends on the history of the system within certain time scales (Pershin and Ventra, 2011). As one kind of memory-circuit elements, memcapacitor has the characteristics of nonlinearity, plasticity, and non-volatility. Nano/Microelectromechanical system (N/MEMS) technology has been used to physically implement memcapacitors (Najem et al., 2019; Liu et al., 2020; Zhao et al., 2020). An N/MEMS parallel-plate capacitor has an elastically suspended upper plate and a fixed lower plate (Martinez-Rincon and Pershin, 2011) and it can exhibit typical memcapacitive characteristics. When some charges are added to the plates, the distance between the parallel plates changes with the charges of the upper and lower plates, which provides a memory mechanism. Generally, the memory effects of memcapacitor originate mainly from two aspects: (1) the change of geometric parameters, e.g., distance and/or shape (Pershin et al., 2015); (2) the change of permittivity, e.g., delayed-response (Martinez-Rincon et al., 2010), permittivity-switching (Driscoll et al., 2009; Lai et al., 2009), and spontaneously polarized medium (Cagin et al., 2007).

Due to the aforementioned memcapacitive characteristics, more and more memcapacitive oscillating circuits have been constructed to explore the nonlinear phenomenon (Yuan et al., 2016; Zhou Z

ORCID: Bei CHEN, https://orcid.org/0000-0002-3383-1279; Bocheng BAO, https://orcid.org/0000-0001-6413-3038

et al., 2017; Rajagopal et al., 2018a, 2018b; Wang XY et al., 2019; Sun et al., 2020). To facilitate numerical simulations and theoretical analysis, some specific mathematical models, such as the Hewlett–Packard (HP) memristor-like model of the memcapacitor (Wang GY et al., 2016), the absolute value function memcapacitor (Yuan et al., 2019b), the logarithmic function memcapacitor (Zhou W et al., 2020), and the fractional-order memcapacitor (Rajagopal et al., 2018a; Akgul, 2019), have been used to characterize memcapacitors. Due to the existence of a line or plane equilibrium set, some unique dynamical phenomena, including state transition, chaos crisis, and multiple coexisting attractors, have been readily discovered in memcapacitive oscillators (Wang GY et al., 2017b; Ma et al., 2020). In addition to the individual memcapacitive oscillators, chaotic circuits constructed with a combination of memristors, memcapacitors, and meminductors can present more diverse dynamical behaviors (Wang XY et al., 2019; Yuan and Li, 2019; Ma et al., 2020). For example, Yuan and Li (2019) constructed a simple chaotic circuit with a memristor, a memcapacitor, and a meminductor connected in parallel and disclosed complex behaviors, including a variable-boostable feature, phase diagram offsets, coexisting multiple attractors, chaotic bursting, and local sustained chaotic states.

Multistability (Pisarchik and Feudel, 2014), i.e., the coexistence of multiple attractors for a set of fixed system parameters, is universal in dynamical systems. On one hand, multistability presents potential threats to engineering systems. On the other hand, the striking phenomenon has potential advantages for some engineering applications, e.g., secure communications (Wang Z et al., 2017; Khorashadizadeh and Majidi, 2018). Hence, multistability has attracted a great deal of interest (Xu et al., 2016, 2020; Chang et al., 2020; Yang et al., 2020). Based on the shape, size, and frequency characteristics of the coexisting attractors, multistability is divided into homogeneous multistability (Li et al., 2018; Yuan et al., 2019b; Bao H et al., 2020a) and extreme multistability (Zhang YZ et al., 2019; Bao H et al., 2020b). In homogeneous multistability, attractors have similar shapes but different sizes and frequencies (Li et al., 2018). However, in extreme multistability, there are coexisting multiple or infinite attractors with different topological structures (Chen et al., 2019b; Zhang YZ et al., 2019). In

addition, the variable-boostable flows commonly exhibit a limited number of coexisting states (Li and Sprott, 2016; Pham et al., 2017; Kingni et al., 2020). When a constant variable controller is employed, the equilibrium points of the variable-boostable system can be adjusted along some special directions, so that the attractors can be repeated with variable offset in the phase space, but the system dynamics remains unchanged (Li and Sprott, 2016).

Different from the variable offset boosting behaviors, the initial conditions of the state variables may induce initial offset boosting coexisting attractors with extreme multistability in some special memristive systems (Wu et al., 2019b; Yuan et al., 2019a). These systems usually have a line, plane, or even space equilibrium set (Bao BC et al., 2016, 2017; Wang GY et al., 2017a) that is related to the memristor inner variable. For example, Bao H et al. (2018) reported a memristive hypogenetic jerk system with a sine memductance. This system has four line equilibrium sets and exhibits periodically initial-condition-dependent boosting behaviors. Wu et al. (2019a) proposed a five-dimensional two-memristor-based dynamical system with a plane equilibrium set and discussed the memristor initial-condition-dependent coexisting plane bifurcations and extreme multistability. In addition, the initial-condition-dependent multistability was found in a hyperchaotic system (Zhang S et al., 2018) and a Hindmarsh–Rose (HR) neuron model (Bao H et al., 2020a) with no equilibrium points. However, there are relatively few studies of extreme multistability of the memcapacitive system (Yuan et al., 2016; Zhou W et al., 2020). Yuan et al. (2016) implemented a memcapacitor-based chaotic oscillator with coexisting attractors triggered by different initial conditions of the state variable. Zhou W et al. (2020) proposed a nonvolatile memcapacitor-aided hyperchaotic oscillator, which could show symmetrical coexisting attractors with the variation of the memcapacitor initial conditions. Nevertheless, the forming mechanism of the coexisting attractors has rarely been discussed.

Inspired by the aforementioned considerations, a charge-controlled memcapacitor model with a cosine function is built in this paper. Based on this model, a four-dimensional (4D) memcapacitive oscillator is constructed. Due to the periodic property of the cosine function, the proposed system is desired to show

the periodically varied initial-condition-switched boosting behaviors. To explore the mechanism of these boosting behaviors, the incremental integral reconstruction method is employed, which has been successfully applied in mechanism analysis of initial-condition-dependent dynamics in some memristive systems (Chen et al., 2018, 2019a, 2020). Using this method, the initial conditions of the original system are converted into the initial-condition-related parameters in the reconstructed dimensionality reduction system, which maintains the same dynamical behaviors of the original system. Thus, the mechanism of the initial-condition-switched boosting behaviors will be reflected in the bifurcation analysis of the initial-condition-related parameters.

2 Memcapacitor model and memcapacitive oscillator

2.1 Mathematical model of the memcapacitor

Some N/MEMS capacitors can exhibit memcapacitive effects (Cagin et al., 2007; Driscoll et al., 2009; Lai et al., 2009; Martinez-Rincon et al., 2010; Martinez-Rincon and Pershin, 2011; Pershin et al., 2015; Najem et al., 2019; Liu et al., 2020; Zhao et al., 2020), and behave like memcapacitors. However, these N/MEMS capacitors usually have complicated nonlinearities, and thus are not convenient for mathematical modeling or theoretical analysis of their application circuits and systems. To effectively demonstrate the memcapacitive effect, a novel charge-controlled memcapacitor with simple nonlinearity is presented in this study and its mathematical model can be described by

$$C_M^{-1}(\sigma) = a + b\cos\sigma, \\ \dot{\sigma} = q, \tag{1}$$

where q is the charge at both ends of the memcapacitor, σ is the time integration of q, and $C_M^{-1}(\sigma)$ stands for the inverse memcapacitor related to σ. As can be observed from Eq. (1), the presented inverse memcapacitance possesses triangular nonlinearity, which is completely different from that reported by Wang GY et al. (2016), Yuan et al. (2019b), and Zhou W et al. (2020).

The memcapacitor parameters in Eq. (1) are set as a=0.18 F^{-1}, b=0.8 F^{-1}·C^{-1}·s^{-1}. When a bipolar periodic stimulus $q(t)=Q_m\sin(2\pi ft)$ is applied, where Q_m=0.5 C, the voltage-charge curves of the memcapacitor with different frequencies (f) and memcapacitor initials ($\sigma(0)$) are plotted in Fig. 1. Fig. 1a shows frequency-dependent pinched hysteresis loops, in which the initial condition $\sigma(0)$ of the memcapacitor is fixed at 0. These hysteresis loops gradually shrink with increasing frequency. When the frequency is 0.5 Hz, the hysteresis loop shrinks almost into a straight line. When the frequency is set as f=0.1 Hz, the pinched hysteresis loops with different nonlinear behaviors are plotted in Fig. 1b by changing the initial condition $\sigma(0)$ of the memcapacitor. With the variation of $\sigma(0)$, the relationship of the voltage and charge of the memcapacitor also changes. It can be predicted that the memcapacitor initials of $\sigma(0)$ may induce the generation of coexisting attractors in the following described memcapacitive oscillator.

2.2 Memcapacitive oscillator

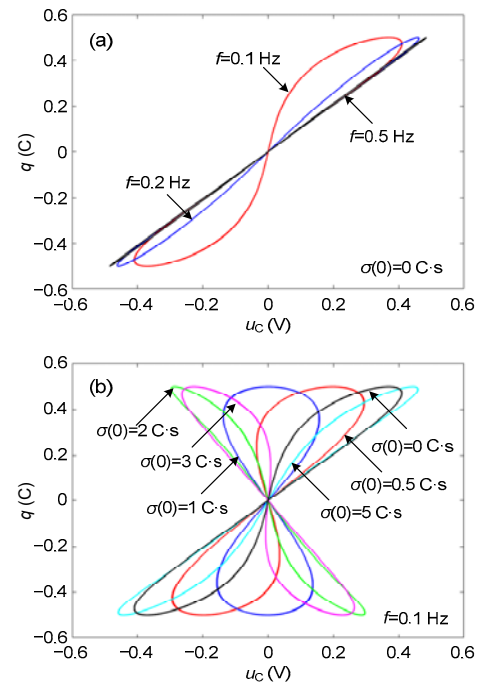To investigate the dynamical behaviors of the aforementioned memcapacitor in its application

Fig. 1 Pinched hysteresis loops of the memcapacitor model: (a) pinched hysteresis loops with $\sigma(0)$=0 C·s; (b) pinched hysteresis loops with f=0.1 Hz
$u_C(t)= C_M^{-1}(\sigma)\,q(t)$ is the terminal voltage of the memcapacitor

circuit, a memcapacitive oscillator is designed and its circuit schematic is shown in Fig. 2. The memcapacitive oscillator is composed of four linear circuit elements and one nonlinear charge-controlled memcapacitor.

The current i_L through the inductor, the voltage v_C across the capacitor, and the charge q_M on memcapacitor are taken as state variables. By applying Kirchoff's laws to this circuit, the state equations are obtained as

$$L\frac{di_L}{dt} = v_C, \tag{2a}$$

$$C\frac{dv_C}{dt} = \frac{1}{R}[(a+b\cos\sigma)q_M - v_C] - i_L, \tag{2b}$$

$$\frac{dq_M}{dt} = \frac{1}{R}v_C + \left(G - \frac{1}{R}\right)(a+b\cos\sigma)q_M, \tag{2c}$$

$$\frac{d\sigma}{dt} = q_M. \tag{2d}$$

To make sure that the unit is one, define

$$x = \frac{Ri_L}{E}, y = \frac{v_C}{E}, z = \frac{q_M}{CE}, u = \frac{\sigma}{RC^2E},$$

$$\tau = \frac{t}{RC}, \mu = \frac{R^2C}{L}, \eta = RC^2E, \tag{3}$$

$$\alpha = Ca, \beta = Cb, \gamma = 1 - RG.$$

Note that the newly introduced parameter E can be used for scaling the amplitudes of the normalized state variables. With the four state variables and six dimensionless parameters defined in Eq. (3), the circuit state equations described by Eq. (2) can be rewritten in a dimensionless form as

$$\dot{x} = \mu y, \tag{4a}$$
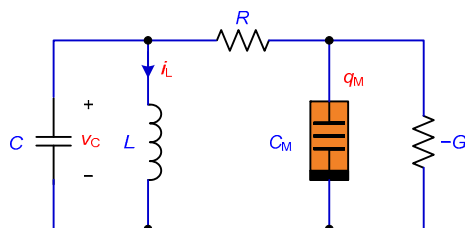$$\dot{y} = -x - y + [\alpha + \beta\cos(\eta u)]z, \tag{4b}$$

Fig. 2 Circuit schematic of the proposed memcapacitive oscillator

$$\dot{z} = y - \gamma[\alpha + \beta\cos(\eta u)]z, \tag{4c}$$
$$\dot{u} = z, \tag{4d}$$

where $\dot{x}=dx/d\tau$, $\dot{y}=dy/d\tau$, $\dot{z}=dz/d\tau$, and $\dot{u}=du/d\tau$. The above ordinary differential equations can be used to describe a 4D dynamical system.

The circuit parameters in Fig. 2 are determined as L=0.13 H, C=3.6 F, R=0.2 Ω, G=2.0 S, the model parameters of the memcapacitor are fixed as a= 0.18 F^{-1}, b=0.8 F^{-1}·C^{-1}·s^{-1}, and the scaling parameter is set to E=2 V. Thus, the dimensionless parameters can be calculated from Eq. (3) as

$$\mu = 1.108, \eta = 5.184,$$
$$\alpha = 0.648, \beta = 2.880, \gamma = 0.6. \tag{5}$$

In the following research, the dimensionless parameters in Eq. (5) remain unchanged.

System (4) has a line equilibrium set S=(0, 0, 0, u_0), which is related to the initial condition of the memcapacitor u_0, i.e., u_0=u(0). This indicates that the positions of the equilibrium points will change with different specified initial conditions of the memcapacitor.

The Jacobian matrix J for system (4) at the line equilibrium set S is derived as

$$J = \begin{bmatrix} 0 & \mu & 0 & 0 \\ -1 & -1 & \alpha + \beta\cos(\eta u_0) & 0 \\ 0 & 1 & -\gamma[\alpha + \beta\cos(\eta u_0)] & 0 \\ 0 & 0 & 1 & 0 \end{bmatrix}. \tag{6}$$

The corresponding eigenpolynomial is deduced as

$$\det(I\lambda - J) = \lambda(\lambda^3 + a_1\lambda^2 + a_2\lambda + a_3) = 0, \tag{7}$$

where

$$\begin{cases} a_1 = 1 + \gamma[\alpha + \beta\cos(\eta u_0)], \\ a_2 = \mu + (\gamma-1)[\alpha + \beta\cos(\eta u_0)], \\ a_3 = \mu\gamma[\alpha + \beta\cos(\eta u_0)]. \end{cases}$$

Apparently, the Jacobian matrix J has one zero root and three non-zero roots. For the three non-zero roots, Routh–Hurwitz conditions are given by

$$a_1 > 0, a_2 > 0, a_3 > 0, \text{ and } a_1a_2 - a_3 > 0. \tag{8}$$

The stability of this line equilibrium set is relevant to the initial condition u_0. Solving the Routh–Hurwitz condition, we have

$$-A < \cos(\eta u_0) < B - A, \qquad (9)$$

where

$$\begin{cases} A = \dfrac{\alpha}{\beta}, \\ B = \dfrac{-(1-\gamma) + \sqrt{(1-\gamma)^2 + 4\gamma(1-\gamma)\mu}}{2\gamma(1-\gamma)\beta}. \end{cases}$$

So, the stable ranges of the line equilibrium set S are derived as

$$-\frac{1}{\eta}\arccos(-A) < u_0 < -\frac{1}{\eta}\arccos(B-A), \quad (10a)$$

$$\frac{1}{\eta}\arccos(B-A) < u_0 < \frac{1}{\eta}\arccos(-A). \quad (10b)$$

If either condition in inequality (10) is satisfied, S is stable; if both conditions of inequality (10) are not satisfied, S is unstable. When the initial condition u_0 increases from $-\pi/\eta$ to π/η, the stability distribution diagram of the line equilibrium set is plotted based on the non-zero eigenvalues of Eq. (7), as shown in Fig. 3. The cyclic width of the stability distribution is $2\pi/\eta$, which can be adjusted by the cyclic width controller η. USF, SNF, HB, and FB represent the unstable saddle-focus, stable node-focus, Hopf bifurcation point, and fold bifurcation point, respectively. The specific values of the Hopf bifurcation points and fold bifurcation points can be derived from inequality (10). Note that USF-1 represents an unstable saddle-focus with two positive real parts and one negative real part, and USF-2 stands for an unstable saddle-focus with one positive real part and two negative real parts.
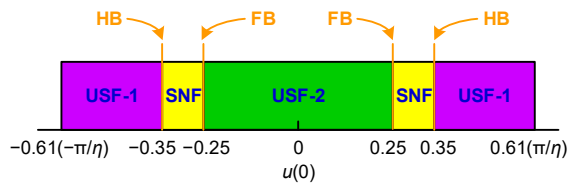

Fig. 3 Stability distribution diagram of the line equilibrium set

USF: unstable saddle-focus; SNF: stable node-focus; HB: Hopf bifurcation point; FB: fold bifurcation point

3 Initial-condition-switched extreme multistability

It has been revealed that the stability distribution of the equilibrium set really depends on the initial conditions of the memcapacitor, which means that the presented memcapacitive oscillator can generate infinitely many coexisting attractors in one cycle. These infinitely many coexisting attractors are switched periodically along the coordinate of the memcapacitor inner variable.

3.1 Periodically repeated bifurcation behaviors

The bifurcation diagrams of state variables x, y, and z are used to describe the dynamical behaviors of system (4). The initial conditions are set to $x(0)=10^{-9}$ and $y(0)=z(0)=0$. These bifurcation diagrams are numerically simulated and plotted in Fig. 4. Herein, the fourth-order Runge–Kutta algorithm with the time step 0.01 and the time-interval [900, 1000] is employed in the numerical simulations.

The bifurcation diagrams in Fig. 4 contain two whole cycles with the variation of $u(0)$. The cyclic width is 1.21 (=$2\pi/\eta$), which is consistent with the stability analysis of the line equilibrium set in Section 2. With the variation of $u(0)$, the bifurcation diagrams of state variables x, y, and z show similar dynamical behaviors, including chaos, chaos crisis, period doubling/halving bifurcations, and stable point.

To explain the periodically repeated dynamical behaviors in Fig. 4, Eq. (4d) is integrated from $-\infty$ to τ:

$$u = \int_{-\infty}^{\tau} z(\xi)\mathrm{d}\xi = u_0 + \int_0^{\tau} z(\xi)\mathrm{d}\xi, \qquad (11)$$

where u_0 is the initial condition of the state variable u, i.e., $u_0 = u(0)$. Denote

$$u_0 = \int_{-\infty}^0 z(\xi)\mathrm{d}\xi. \qquad (12)$$

Then, system (4) can be rewritten as

$$\begin{cases} \dot{x} = \mu y, \\ \dot{y} = -x - y + \left[\alpha + \beta\cos\left(\eta u_0 + \eta\int_0^{\tau} z(\xi)\mathrm{d}\xi\right)\right]z, \\ \dot{z} = y - \gamma\left[\alpha + \beta\cos\left(\eta u_0 + \eta\int_0^{\tau} z(\xi)\mathrm{d}\xi\right)\right]z. \end{cases} \quad (13)$$

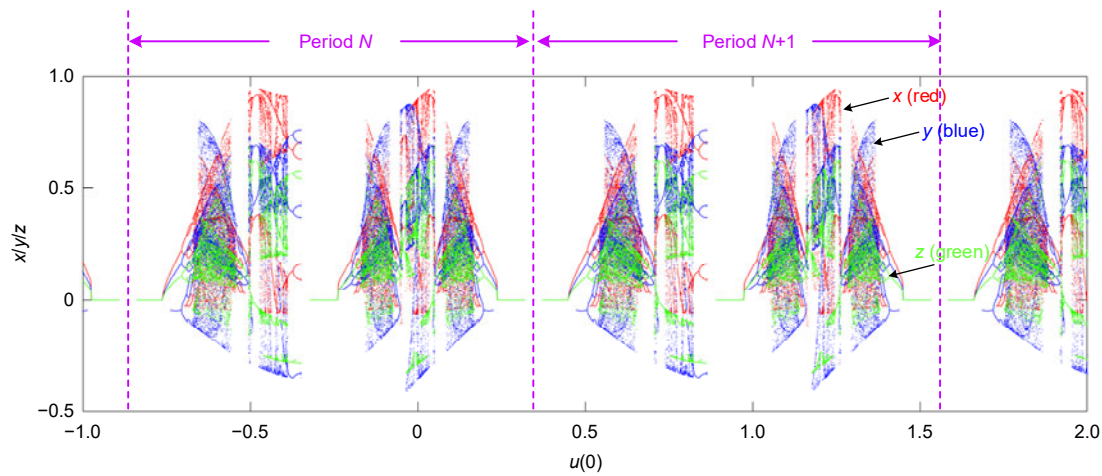Thus, the initial condition u_0 is explicitly expressed in Eq. (13).

Fig. 4 Initial $u(0)$ relied bifurcation diagrams of state variables x, y, and z with other fixed initial conditions $x(0)=10^{-9}$, $y(0)=z(0)=0$ (References to color refer to the online version of this figure)

Suppose

$$u_0 = u_{00} \pm 2n\pi/\eta, \qquad (14)$$

where n is a natural number and u_{00} is an initial condition compensation that satisfies the following condition (Bao H et al., 2020a):

$$-\pi/\eta < u_{00} + \int_0^\tau z(\xi)\mathrm{d}\xi < \pi/\eta. \qquad (15)$$

Because

$$
\begin{aligned}
&\cos\left(\eta u_0 + \eta\int_0^\tau z(\xi)\mathrm{d}\xi\right) \\
&= \cos\left(\eta u_{00} \pm 2n\pi + \eta\int_0^\tau z(\xi)\mathrm{d}\xi\right) \qquad (16) \\
&= \cos\left(\eta u_{00} + \eta\int_0^\tau z(\xi)\mathrm{d}\xi\right),
\end{aligned}
$$

by substituting Eq. (14) into Eq. (13), Eq. (13) still holds. It is easy to deduce that different initial u_0 can induce infinite coexisting attractors along the u coordinate, and these coexisting attractors are periodically repeated with the fixed cycle length of $2\pi/\eta$, implying the occurrence of the initial-condition-switched boosting extreme multistability in Fig. 4.

The bifurcation diagram of state variable y and the first three Lyapunov exponents in a whole period of Fig. 4 are drawn in Figs. 5a and 5b, respectively. At $u(0)=-0.76$ and -0.71, two period doubling bifurcations occur, which makes the system trajectories
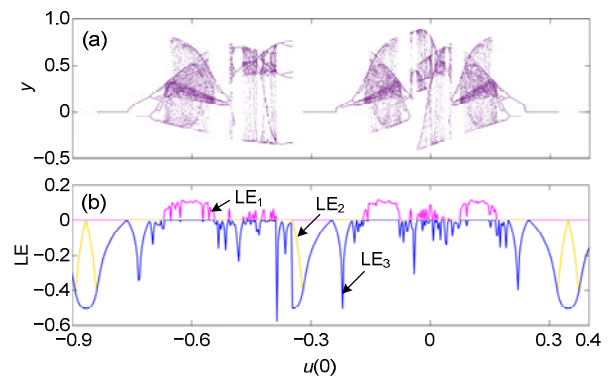

Fig. 5 Bifurcation diagram of the state variable y (a) and the first three Lyapunov exponents (b) in period N of Fig. 4

transmit from the period-1 to period-2 limit cycle, and then to the period-4 limit cycle successively, whereas for $u(0)=0.18$ and 0.20, two period halving bifurcations occur and the system trajectory transmits from the period-4 limit cycle to the period-2 limit cycle, and then to the period-1 limit cycle. Obviously, the dynamical behaviors revealed by the bifurcation diagram are the same as those disclosed by the Lyapunov exponents. The bifurcation plots reveal relatively complete period doubling/halving bifurcation routes with the variation of memcapacitor initial $u(0)$, which illustrates the generation of extreme multistability in system (4).

In addition to the initial condition of the memcapacitor inner variable, the initial conditions of the other state variables can promote periodic repetition of bifurcation behaviors. Fig. 6 shows the bifurcation

diagrams of the state variable y with the variation of initial conditions $x(0)$ and $z(0)$. In Fig. 6a, five complete cycles are plotted in the range of $x(0)=[-1, 2]$, whose cyclic width is approximately measured as 0.52. In Fig. 6b, six complete cycles are observed within $z(0)=[-1, 2]$ and the cyclic width is approximately 0.47. Each cycle has the same bifurcation behavior, confirming the generation of the initial-condition-switched boosting extreme multistability. However, as the initial condition $y(0)$ changes, the dynamical behavior of system (4) is constant, which is not plotted.

3.2 Initial-condition-switched offset boosting attractors

In addition to periodicity, the period doubling/halving bifurcations in Figs. 4 and 5 indicate the existence of coexisting attractors in system (4). The representative coexisting attractors in an individual varying cycle are depicted in Figs. 7a and 7b. In Fig. 7a, the chaotic attractors with different topological structures triggered from different memcapacitor initial conditions are displayed. The red and magenta curves show a pair of symmetrical chaotic attractors, and the yellow curve presents a double-scroll chaotic attractor, whereas in Fig. 7b, a stable point and three limit cycles with period-1, period-2, and period-4 for different memcapacitor initial conditions are plotted. The phase portraits of the coexisting attractors in

three adjacent periods are depicted in Fig. 7c. The chaotic attractors at $u(0)=0.558$ and $u(0)=1.210$ and their periodically boosted attractors along the u coordinate are illustrated. Therefore, the initial-condition-switched boosting behaviors of the attractor positions along the u coordinate are revealed. It is also obvious that the attractors appear periodically with the cyclic width $2\pi/\eta$ in system (4).

The mean values of state variables are plotted with respect to $u(0)$ in Fig. 8. Note that the boosting route is nonlinear and one-dimensional. The attractors are moving nonlinearly along the positive direction of the u coordinate with different topological structures, which is consistent with the initial-condition-switched boosting behaviors presented in Fig. 7.

To investigate the initial-condition-switched boosting behaviors related to other initial conditions, the mean values of the four state variables and the corresponding phase portraits under $(x(0), 10^{-9}, 0, 0)$ and $(10^{-9}, 0, z(0), 0)$ are plotted in Fig. 9. In Fig. 9a, the generated attractors are periodically boosted by $x(0)$ along the negative direction of the u coordinate. In Fig. 9b, the generated attractors are periodically boosted by $z(0)$ along the positive direction of the u coordinate. In addition to the attractor positions, the attractor types are varied with the change of $x(0)$ and $z(0)$. The evolution patterns of dynamical behaviors and the measured cyclic widths are consistent with those revealed by the bifurcation plots in Fig. 6.
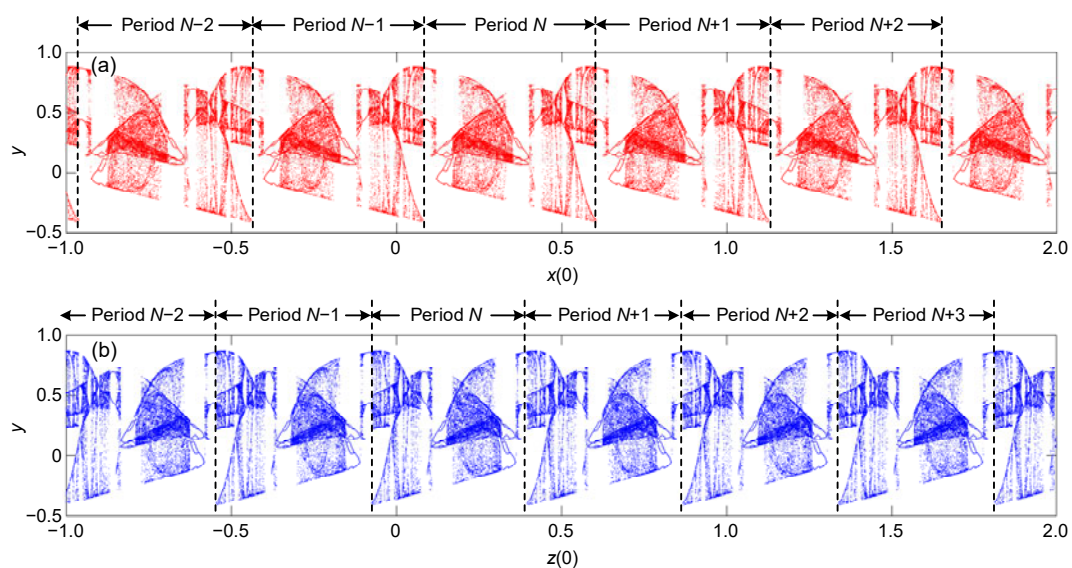

Fig. 6 Bifurcation diagrams of the state variable *y* with respect to *x*(0) and *z*(0): (a) *x*(0) related bifurcation diagram with fixed *y*(0)=10⁻⁹, *z*(0)=*u*(0)=0; (b) *z*(0) related bifurcation diagram with fixed *x*(0)=10⁻⁹, *y*(0)=*u*(0)=0
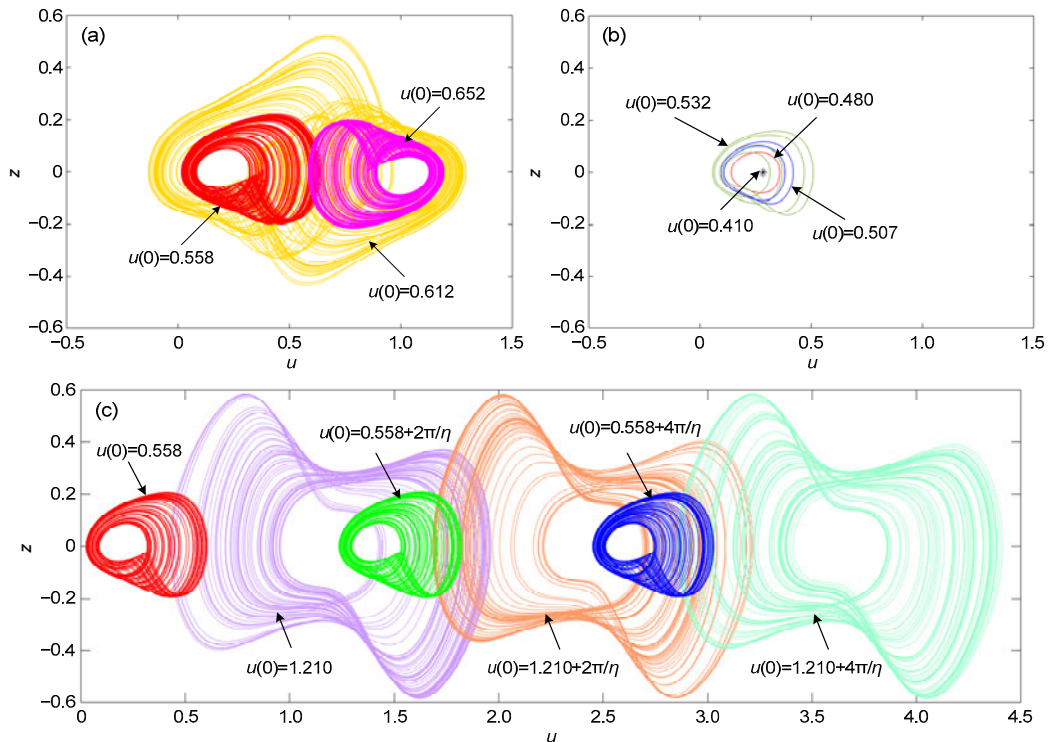
Fig. 7   Initial $u(0)$ dependent coexisting behaviors and initial-condition-switched boosting behaviors with fixed $x(0)=10^{-9}$, $y(0)=z(0)=0$: (a) coexisting chaotic attractors in an individual period, where the left spiral attractor (red), right spiral attractor (magenta), and double-scroll attractor (yellow) correspond to $u(0)=0.558$, 0.652, and 0.612, respectively; (b) coexisting point and periodic attractors in an individual period, where the stable point (black), period-1 limit cycle (red), period-2 limit cycle (blue), and period-4 limit cycle (dark green) correspond to $u(0)=0.410$, 0.480, 0.507, and 0.532, respectively; (c) initial offset-boosted coexisting attractors in three adjacent periods, where the red, green, and blue spiral attractors correspond to $u(0)=0.558$, $0.558+2\pi/\eta$, and $0.558+4\pi/\eta$, respectively, and the lavender, dark orange, and light green chaotic attractors correspond to $u(0)=1.210$, $1.210+2\pi/\eta$, and $1.210+4\pi/\eta$, respectively. References to color refer to the online version of this figure
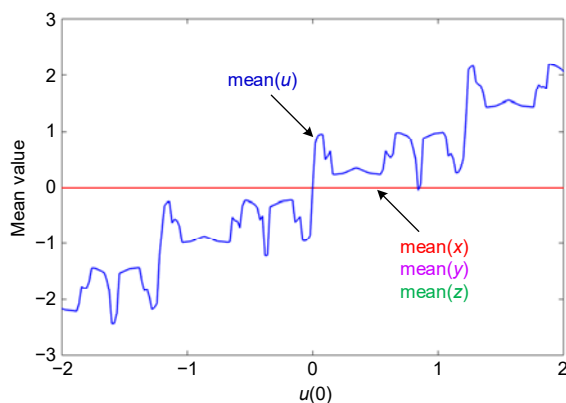

Fig. 8   Mean values of four state variables with the fixed initial conditions $x(0)=10^{-9}$ and $y(0)=z(0)=0$, where mean(x), mean(y), and mean(z) are all equal to 0, while mean(u) increases nonlinearly

From Figs. 8 and 9, it is shown that the initial conditions $x(0)$, $z(0)$, and $u(0)$ can all behave as the

boosting adjusters. According to the line equilibrium set $S=(0, 0, 0, u_0)$, the positions of equilibrium points change with $u(0)$, resulting in the change of attractor positions. The coupling effect among the state variables in system (4) indicates the periodic evolution of coexisting attractors related to the initial conditions $x(0)$ and $z(0)$. The mechanism of the initial-condition-switched boosting extreme multistability is presented in the following section.

4   Mechanism of the initial-condition-switched boosting behaviors

4.1   Reconstructed system via time integral transformation

To explain the forming mechanism of the initial-condition-switched boosting behaviors related to

extreme multistability, a three-dimensional (3D) dimensionality reduction model is derived. For the convenience of description, three new state variables and four initial-condition-related parameters are introduced as follows (Chen et al., 2018, 2019a, 2020):
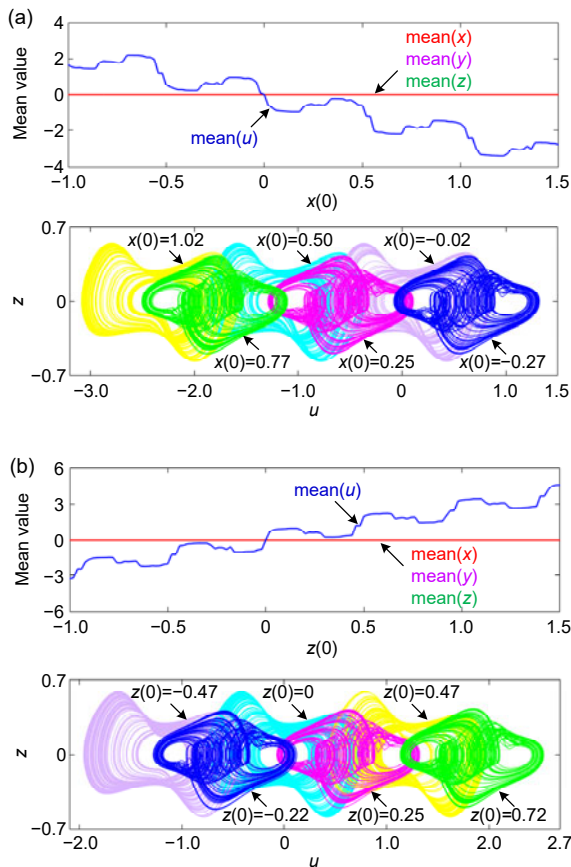

Fig. 9 Initial-condition-switched boosting behaviors illustrated by the mean values of the four state variables and the corresponding phase portraits: (a) the mean values of the four state variables (top) and $x(0)$-switched boosting behaviors (bottom) with fixed $y(0)=10^{-9}$ and $z(0)=u(0)=0$. In the top figure, mean(x), mean(y), and mean(z) are all equal to 0, while mean(u) decreases nonlinearly. In the bottom figure, the single-scroll chaotic attractors for $x(0)=1.02$, 0.50, and −0.02 as well as the double-scroll chaotic attractors for $x(0)=0.77$, 0.25, and −0.27 are all boosted with initial-offset −0.52 along the u coordinate; (b) the mean values of the four state variables (top) and $z(0)$-switched boosting behaviors (bottom) with fixed $x(0)=10^{-9}$ and $y(0)=u(0)=0$. In the top figure, mean(x), mean(y), and mean(z) are all equal to 0, while mean(u) increases nonlinearly. In the bottom figure, the single-scroll chaotic attractors for $z(0)=−0.47$, 0, and 0.47 as well as the double-scroll chaotic attractors for $z(0)= −0.22$, 0.25, and 0.72 are boosted with initial-offset 0.47 along the u coordinate

$$X = \int_0^t x\,\mathrm{d}\tau, \quad Y = \int_0^t y\,\mathrm{d}\tau, \quad Z = \int_0^t z\,\mathrm{d}\tau, \quad (17)$$

$$\eta_0 = u(0), \quad \eta_1 = x(0), \quad \eta_2 = y(0), \quad \eta_3 = z(0). \quad (18)$$

Transforming by incremental integration from 0 to t, the equations of system (4) are rewritten as

$$\begin{cases} \dot{X} = \mu Y + \eta_1, \\ \dot{Y} = -X - Y + \alpha Z + \dfrac{\beta}{\eta}\sin(\eta Z + \eta\eta_0) - \dfrac{\beta}{\eta}\sin(\eta\eta_0) + \eta_2, \\ \dot{Z} = Y - \gamma\alpha Z - \dfrac{\gamma\beta}{\eta}\sin(\eta Z + \eta\eta_0) + \dfrac{\gamma\beta}{\eta}\sin(\eta\eta_0) + \eta_3. \end{cases}$$
$$(19)$$

The new 3D system (19) possesses the four parameters (η_0, η_1, η_2, and η_3) related to the initial conditions of system (4). These explicitly expressed initial-condition-related parameters help us interpret the dynamical mechanism of the revealed initial-condition-switched boosting behaviors.

According to Eq. (17), the initial conditions of system (19) all equal to 0, i.e., $X(0)=0$, $Y(0)=0$, and $Z(0)=0$. In this case, the reconstructed system can retain the same dynamical behaviors of system (4).

The equilibrium point of system (19) is determined by solving the following equations:

$$\begin{cases} 0 = \mu Y + \eta_1, \\ 0 = -X - Y + \alpha Z + \dfrac{\beta}{\eta}\sin(\eta Z + \eta\eta_0) - \dfrac{\beta}{\eta}\sin(\eta\eta_0) + \eta_2, \\ 0 = Y - \gamma\alpha Z - \dfrac{\gamma\beta}{\eta}\sin(\eta Z + \eta\eta_0) + \dfrac{\gamma\beta}{\eta}\sin(\eta\eta_0) + \eta_3. \end{cases}$$
$$(20)$$

The equilibrium point of system (19) is expressed as

$$\boldsymbol{P} = \left(-\frac{1-\gamma}{\mu\gamma}\eta_1 + \eta_2 + \frac{1}{\gamma}\eta_3, -\frac{\eta_1}{\mu}, \hat{Z} \right), \quad (21)$$

where $\hat{Z}$ is the root of the following equation:

$$\alpha Z + \frac{\beta}{\eta}\sin(\eta Z + \eta\eta_0) = \frac{\beta}{\eta}\sin(\eta\eta_0) - \frac{1}{\mu\gamma}\eta_1 + \frac{1}{\gamma}\eta_3. \quad (22)$$

Obviously, $\hat{Z}$ is determined by η_0, η_1, and η_3.

The Jacobian matrix $\boldsymbol{J}_{\mathrm{D}}$ for the dimensionality

reduction system (19) at the equilibrium point P is deduced as

$$J_\mathrm{D} = \begin{bmatrix} 0 & \mu & 0 \\ -1 & -1 & \alpha + \beta \cos(\eta \hat{Z} + \eta \eta_0) \\ 0 & 1 & -\gamma \alpha - \gamma \beta \cos(\eta \hat{Z} + \eta \eta_0) \end{bmatrix}. \quad (23)$$

So, the characteristic polynomial equation is derived as

$$\det(\boldsymbol{I}\lambda - \boldsymbol{J}_\mathrm{D}) = \lambda^3 + b_1 \lambda^2 + b_2 \lambda + b_3 = 0, \quad (24)$$

where

$$\begin{cases} b_1 = 1 + \gamma[\alpha + \beta \cos(\eta \hat{Z} + \eta \eta_0)], \\ b_2 = \mu + (\gamma - 1)[\alpha + \beta \cos(\eta \hat{Z} + \eta \eta_0)], \\ b_3 = \mu \gamma [\alpha + \beta \cos(\eta \hat{Z} + \eta \eta_0)]. \end{cases}$$

Obviously, the stability of P is related to η_0 and $\hat{Z}$. In other words, the initial-condition-related parameters η_0, η_1, η_2, and η_3 have a significant impact on the stability of the equilibrium point P and thereby affect the dynamical behaviors.

4.2 Parameter-switched boosting behaviors

The initial-condition-related parameters are determined as $\eta_1=10^{-9}$ and $\eta_2=\eta_3=0$, and the initial conditions of system (19) are fixed as $X(0)=Y(0)=Z(0)=0$. When increasing η_0, the bifurcation diagram of the state variable Y and the first two Lyapunov exponents are together given in Fig. 10. Comparing Fig. 10 with Fig. 5, the dimensionality reduction system (19) reveals the same dynamic behaviors as system (4).
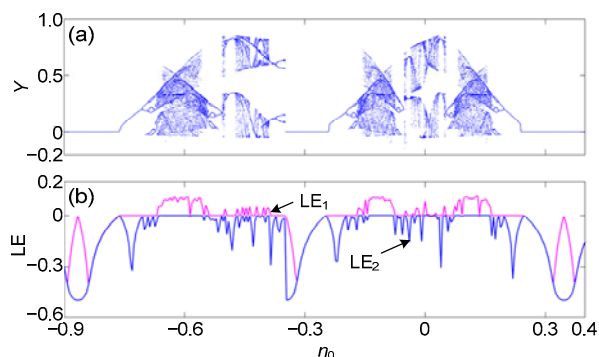

Fig. 10 The initial-condition-related parameter η_0 relied bifurcation diagram of the state variable Y (a) and the first two Lyapunov exponents (b) of system (19) with fixed $X(0)=Y(0)=Z(0)=0$, $\eta_1=10^{-9}$, and $\eta_2=\eta_3=0$

When $\eta_1=10^{-9}$ and $\eta_2=\eta_3=0$ are assigned, the reconstructed chaotic and periodic attractors of the dimensionality reduction system (19) are shown in Fig. 11. According to the initial conditions used in Figs. 7a and 7c, Fig. 11a shows four reconstructed chaotic attractors under η_0=0.558, 0.612, 0.652, and 1.210. Meanwhile, corresponding to the periodic coexisting attractors depicted in Fig. 7b, one reconstructed point attractor and three reconstucted period-1, period-2, and period-4 limit cycles are obtained under η_0=0.410, 0.480, 0.507, and 0.532, as shown in Fig. 11b.

When each of the four initial-condition-related parameters is chosen as the boosting controller sequentially, the dynamical behaviors of the dimensionality reduction system (19) are discussed as follows:

Case 1: η_0 is the boosting controller with fixed $\eta_1=10^{-9}$ and $\eta_2=\eta_3=0$

Because $\eta_1=10^{-9}\approx 0$ and $\eta_2=\eta_3=0$, the equilibrium point is expressed as $P=(0, 0, \hat{Z})$. Fig. 12a shows that with the variation of η_0, $\hat{Z}$ expresses the periodic changing rule. Thus, the equilibrium point P periodically moves around the origin of the Z coordinate with the same cyclic width $2\pi/\eta$ as the original system (4). The mean values of the state variables are plotted with respect to η_0 in the top of Fig. 13a. Through reconstruction, the mean value of Z changes periodically around zero, and the mean values of X and Y remain at zero. Thus, the initial-condition-switched boosting behaviors disappear in the reconstructed system (19). The bifurcation diagrams in the bottom of Fig. 13a confirm these behaviors. Therefore, the different attractors triggered by the initial-condition-related parameter η_0 with the $2\pi/\eta$ interval drop into the same region in the phase plane, which is different from the boosting phenomenon in Fig. 7c.

Case 2: η_1 is the boosting controller with fixed $\eta_2=10^{-9}$ and $\eta_3=\eta_0=0$

The equilibrium point of system (19) is expressed as $P=[-(1-\gamma)\eta_1/(\mu\gamma), -\eta_1/\mu, \hat{Z}]$. The trajectory of $\hat{Z}$ is plotted with respect to the initial-condition-related parameter η_1 in Fig. 12b, which manifests that the equilibrium point P periodically moves along the negative direction of the Z coordinate as η_1 increases. Also, the X and Y coordinates of P decrease linearly. These features are also reflected by the mean values of the three state variables given
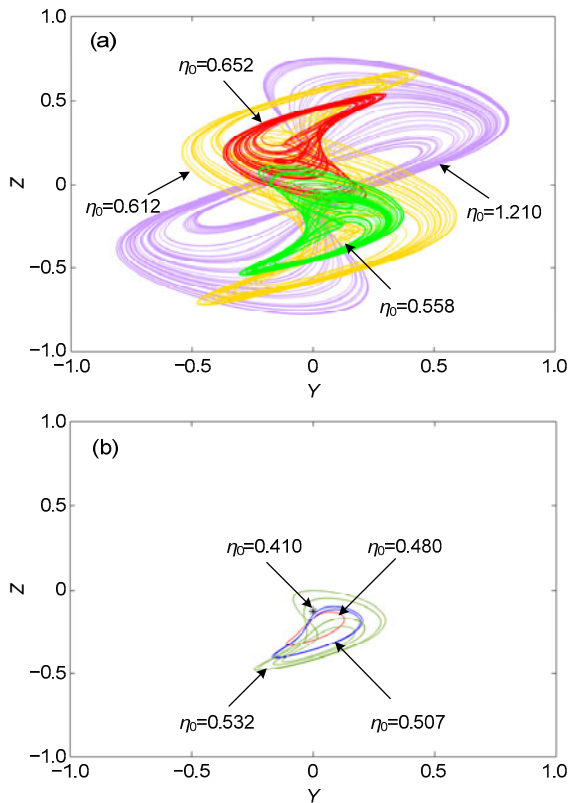
Fig. 11 The initial-condition-switched coexisting attractors of the dimensionality reduction system with fixed $X(0)=Y(0)=Z(0)=0$, $\eta_1=10^{-9}$, and $\eta_2=\eta_3=0$: (a) chaotic behaviors with $\eta_0=0.558/0.612/0.652/1.210$; (b) periodic behaviors with $\eta_0=0.410/0.480/0.507/0.532$

Fig. 12 Trajectories of $\hat{Z}$ with the variation of the initial parameters η_0, η_1, η_2, and η_3: (a) $\eta_1=10^{-9}$ and $\eta_2=\eta_3=0$; (b) $\eta_2=10^{-9}$ and $\eta_3=\eta_0=0$; (c) $\eta_1=10^{-9}$ and $\eta_3=\eta_0=0$; (d) $\eta_1=10^{-9}$ and $\eta_2=\eta_0=0$

in the top of Fig. 13b. The mean value of Z decreases periodically, but the mean values of X and Y decrease linearly, leading to the periodic evolution and offset boosting features of the bifurcation behaviors. These characteristics are further confirmed by the bifurcation diagram depicted in the bottom of Fig. 13b. Besides, the periodic evolution of dynamical behaviors has the same cyclic width 0.52 as that in Fig. 6a.

Case 3: η_2 is the boosting controller with fixed $\eta_1=10^{-9}$ and $\eta_3=\eta_0=0$

The equilibrium point of system (19) is expressed as $\boldsymbol{P}=(\eta_2, 0, \hat{Z})$. The trajectory of $\hat{Z}$ is plotted with respect to the initial-condition-related parameter η_2 in Fig. 12c. As η_2 increases, the Y and Z coordinates of $\boldsymbol{P}$ remain at zero and the X coordinate increases linearly. In the top of Fig. 13c, the evolution of the state mean values is plotted with respect to η_2, which agrees with the evolution of the equilibrium point $\boldsymbol{P}$. The bifurcation diagram given in the bottom
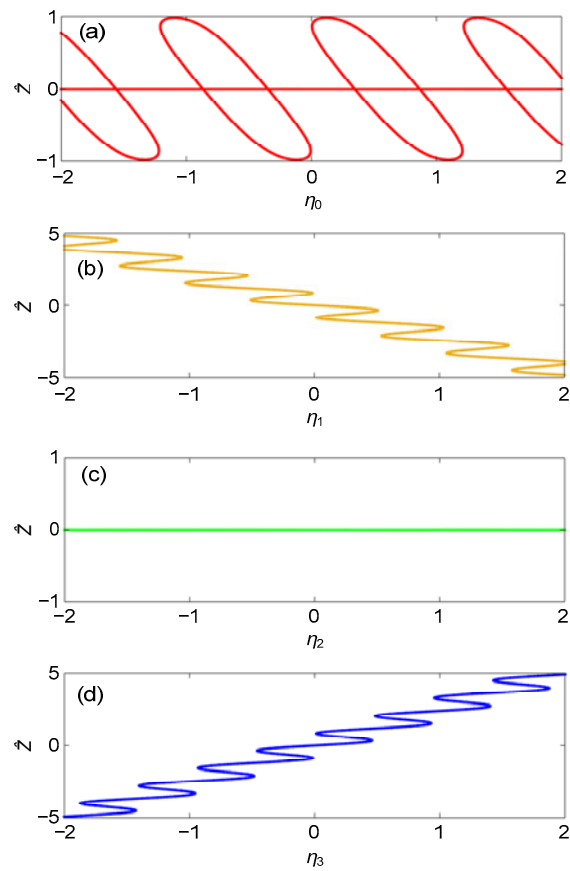
of Fig. 13c shows that system (19) always operates in the chaotic mode with the variation of η_2. However, these chaotic attractors are linearly boosted along the positive direction of the X coordinate, because the X coordinate of $\boldsymbol{P}$ is linearly changed with η_2.

Case 4: η_3 is the boosting controller with fixed $\eta_1=10^{-9}$ and $\eta_2=\eta_0=0$

The equilibrium point of system (19) is expressed as $\boldsymbol{P}=(\eta_3/\gamma, 0, \hat{Z})$. Combined with Fig. 12d, we can conclude that as η_3 increases, $\boldsymbol{P}$ increases linearly along the X coordinate, remains at zero along the Y coordinate, and periodically increases in the positive direction of the Z coordinate. The evolution of $\boldsymbol{P}$ induces the movement of the attractors' positions. These are also presented by the state mean values and bifurcation diagram in Fig. 13d. The revealed behaviors are similar to those depicted in Fig. 13b, but the boosting direction and the evolution period are
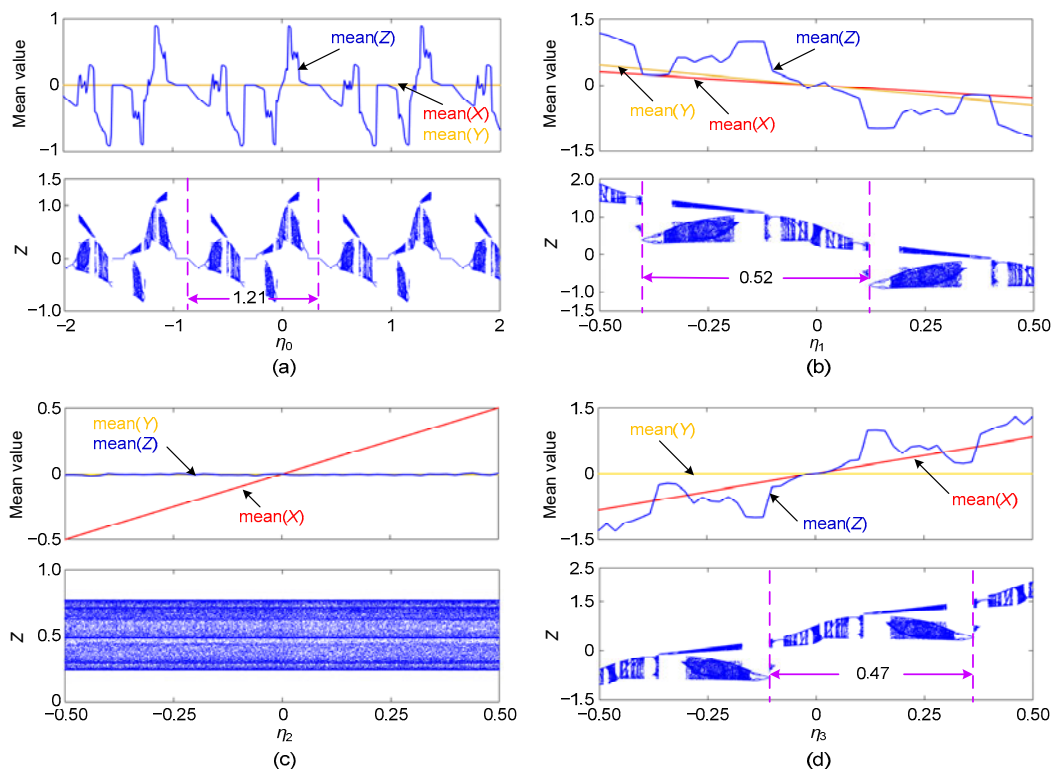
Fig. 13 Initial parameter-switched boosting behaviors of the dimensionality reduction system illustrated by the state mean values and bifurcation diagrams: (a) η_0-switched boosting behavior with $\eta_1=10^{-9}$ and $\eta_2=\eta_3=0$; (b) η_1-switched boosting behavior with $\eta_2=10^{-9}$ and $\eta_3=\eta_0=0$; (c) η_2-switched boosting behavior with $\eta_1=10^{-9}$ and $\eta_3=\eta_0=0$; (d) η_3-switched boosting behavior with $\eta_1=10^{-9}$ and $\eta_2=\eta_0=0$

different. The period of the bifurcation behaviors is 0.47, which is the same as that in Fig. 6b.

The veil of the initial-condition-switched boosting behaviors induced by the initial conditions $x(0)$, $y(0)$, $z(0)$, and $u(0)$ in system (4) can be uncovered in system (19). The initial conditions of state variables x, y, z, and u in system (4) are transformed into the initial-condition-related parameters η_1, η_2, η_3, and η_0 in system (19). Thus, the mechanism of the initial-condition-switched boosting behaviors is explained by the analysis of the dynamical behaviors associated with the initial-condition-related parameters.

5 Circuit simulation for the reconstructed system

The implementation circuit of the dimensionality reduction system (19) is shown in Fig. 14. This circuit is composed of operational amplifiers, trigonometric function converters, resistors, and capacitors.

The time constant of this circuit is defined as $RC=$ 10 kΩ×33 nF=0.33 ms. Then the other resistors are calculated as $R_1=R/\mu$=9.03 kΩ, $R_2=R/\alpha$=15.43 kΩ, $R_3=\eta R/\beta$=18 kΩ, $R_4=\eta R$=51.84 kΩ, $R_5=R/(\gamma\alpha)$= 25.72 kΩ, and $R_6=\eta R/(\gamma\beta)$=30 kΩ.

Following the implementation circuit in Fig. 14, the circuit equations of the dimensionality reduction system (19) are expressed as

$$RC\frac{\mathrm{d}v_x}{\mathrm{d}t} = \frac{R}{R_1}v_y + V_1, \tag{25a}$$

$$\begin{aligned} RC\frac{\mathrm{d}v_y}{\mathrm{d}t} &= \frac{R}{R_2}v_z + \frac{R}{R_3}\sin\left(\frac{R_4}{R}v_z + \frac{R_4}{R}V_0\right) \\ &\quad -v_x - v_y - \frac{R}{R_3}\sin\left(\frac{R_4}{R}V_0\right) + V_2, \end{aligned} \tag{25b}$$

$$\begin{aligned} RC\frac{\mathrm{d}v_z}{\mathrm{d}t} &= -\frac{R}{R_5}v_z - \frac{R}{R_6}\sin\left(\frac{R_4}{R}v_z + \frac{R_4}{R}V_0\right) \\ &\quad +v_y + \frac{R}{R_6}\sin\left(\frac{R_4}{R}V_0\right) + V_3, \end{aligned} \tag{25c}$$

where v_x, v_y, and v_z are three circuit variables corresponding to the state variables of system (19), and four DC voltage biases V_0–V_3 are corresponding to the initial-condition-related parameters η_0–η_3.

Let $V_1=10^{-9}$ V and $V_2=V_3=0$ V. When V_0 is set to 0.558, 0.612, 0.652, or 1.210 V, the Power SIMulation (PSIM) circuit simulations are depicted in Fig. 15a. The chaotic attractors with four different topological structures emerge around the original point. Then, the limit cycles with period-1, period-2, and period-4 for $V_0=0.480$, 0.507, and 0.532 V are plotted in Fig. 15b. The PSIM circuit simulation results match well with the MATLAB numerical simulation results in Fig. 11. These results for different values of V_0–V_3 can further confirm the infinite coexisting attractors' behaviors.

6 Conclusions

The initial-condition-switched boosting behaviors can exhibit the periodical coexisting attractors with different topological structures and positions along the coordinate of the memcapacitor inner variable. In this paper, we have introduced a cosine memcapacitor into an oscillator, and thus presented a 4D memcapacitive oscillator. The 4D memcapacitive oscillator possessed a line equilibrium set, and its stability periodically evolved with the initial condition of the memcapacitor. These characteristics could induce complex dynamical behaviors in the 4D memcapacitive oscillator. By employing multiple numerical simulation methods, the initial-condition-related complex dynamical behaviors have been
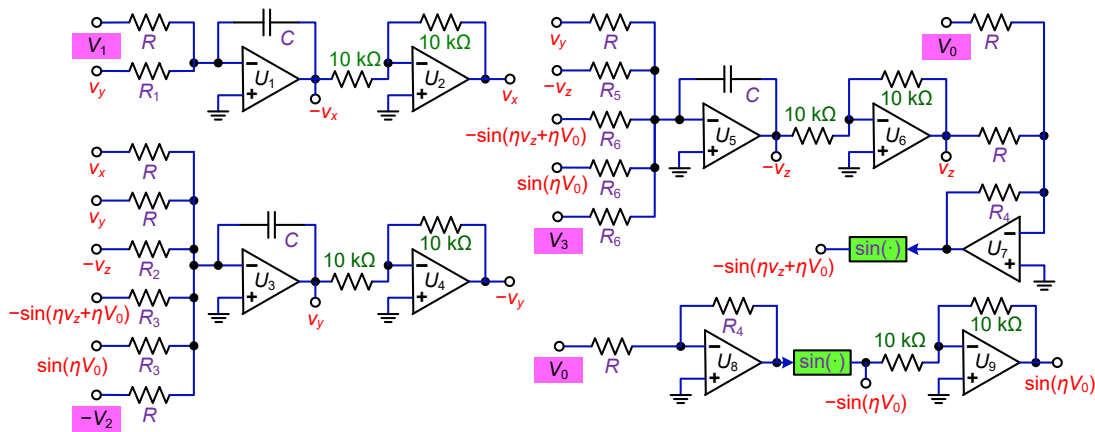

Fig. 14 Analog implementation circuit for the dimensionality reduction system
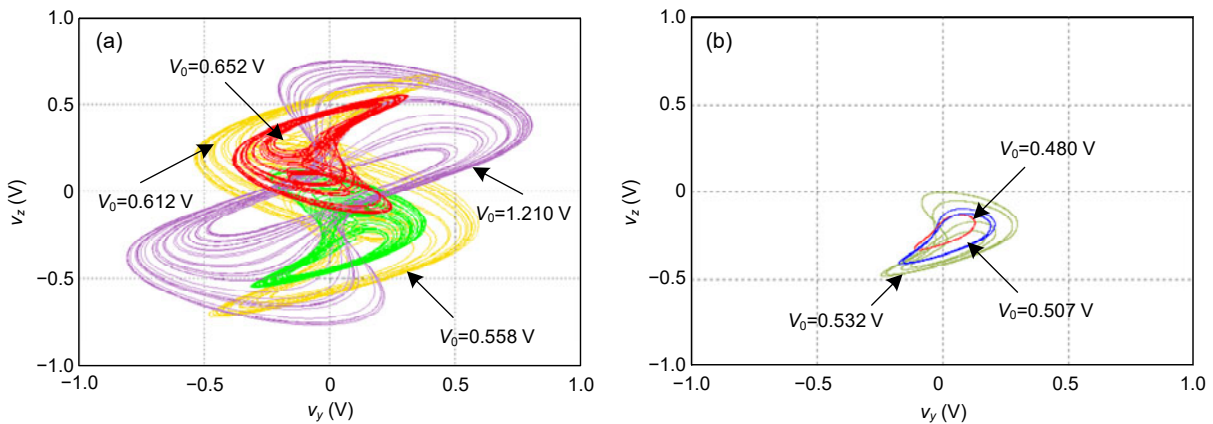

Fig. 15 Power SIMulation (PSIM) circuit simulations of the dimensionality reduction system for different initial conditions: (a) chaotic behaviors with $V_0=0.558/0.612/0.652/1.210$ V, $V_1=10^{-9}$ V, and $V_2=V_3=0$ V; (b) periodic behaviors with $V_0=0.480/0.507/0.532$ V, $V_1=10^{-9}$ V, and $V_2=V_3=0$ V

disclosed. In particular, the initial-condition-switched boosting extreme multistability has been revealed. Furthermore, the mechanism of the initial-condition-switched boosting behaviors was uncovered based on a reduced-order system constructed by the integral transformation. The obtained results have been further confirmed by the PSIM circuit simulations. The revealed initial-condition-switched boosting extreme multistability has more potential applications in secure communications (Wang Z et al., 2017; Khorashadizadeh and Majidi, 2018) and deserves our future study.

Contributors

Bocheng BAO designed the research. Bei CHEN and Quan XU processed the data. Bei CHEN drafted the paper. Quan XU and Mo CHEN helped organize the paper. Huagan WU and Bocheng BAO revised and finalized the paper.

Compliance with ethics guidelines

Bei CHEN, Quan XU, Mo CHEN, Huagan WU, and Bocheng BAO declare that they have no conflict of interest.

References

Akgul A, 2019. Chaotic oscillator based on fractional order memcapacitor. *J Circ Syst Comput*, 28(14):1950239. https://doi.org/10.1142/S0218126619502396

Bao BC, Xu Q, Bao H, et al., 2016. Extreme multistability in a memristive circuit. *Electron Lett*, 52(12):1008-1010. https://doi.org/10.1049/el.2016.0563

Bao BC, Jiang T, Wang GY, et al., 2017. Two-memristor-based Chua's hyperchaotic circuit with plane equilibrium and its extreme multistability. *Nonl Dynam*, 89(2):1157-1171. https://doi.org/10.1007/s11071-017-3507-0

Bao H, Wang N, Bao BC, et al., 2018. Initial condition-dependent dynamics and transient period in memristor-based hypogenetic jeck system with four line equilibria. *Commun Nonl Sci Nemer Simul*, 57:264-275. https://doi.org/10.1016/j.cnsns.2017.10.001

Bao H, Chen M, Wu HG, et al., 2020a. Memristor initial-boosted coexisting plane bifurcations and its extreme multi-stability reconstitution in two-memristor-based dynamical system. *Sci China Technol Sci*, 63(4):603-613. https://doi.org/10.1007/s11431-019-1450-6

Bao H, Liu WB, Ma J, et al., 2020b. Memristor initial-offset boosting in memristive HR neuron model with hidden firing patterns. *Int J Bifurc Chaos*, 30(10):2030029. https://doi.org/10.1142/S0218127420300293

Cagin E, Chen DY, Siddiqui JJ, et al., 2007. Hysteretic metal-ferroelectric-semiconductor capacitors based on PZT/ZnO heterostructures. *J Phys D Appl Phys*, 40(8):2430-2434. https://doi.org/10.1088/0022-3727/40/8/003

Chang H, Li YX, Chen GR, et al., 2020. Extreme multistability and complex dynamics of a memristor-based chaotic

system. *Int J Bifurc Chaos*, 30(8):2030019. https://doi.org/10.1142/S0218127420300190

Chen M, Feng Y, Bao H, et al., 2018. State variable mapping method for studying initial-dependent dynamics in memristive hyper-jerk system with line equilibrium. *Chaos Sol Fract*, 115:313-324. https://doi.org/10.1016/j.chaos.2018.07.025

Chen M, Feng Y, Bao H, et al., 2019a. Hybrid state variable incremental integral for reconstructing extreme multistability in memristive jerk system with cubic nonlinearity. *Complexity*, 2019:8549472. https://doi.org/10.1155/2019/8549472

Chen M, Ren X, Wu HG, et al., 2019b. Periodically varied initial offset boosting behaviors in a memristive system with cosine memductance. *Front Inform Technol Electron Eng*, 20(12):1706-1716. https://doi.org/10.1631/FITEE.1900360

Chen M, Ren X, Wu HG, et al., 2020. Interpreting initial offset boosting via reconstitution in integral domain. *Chaos Sol Fract*, 131:109544. https://doi.org/10.1016/j.chaos.2019.109544

Driscoll T, Kim HT, Chae BG, et al., 2009. Memory metamaterials. *Science*, 325(5947):1518-1521. https://doi.org/10.1126/science.1176580

Khorashadizadeh S, Majidi MH, 2018. Synchronization of two different chaotic systems using Legendre polynomials with applications in secure communications. *Front Inform Technol Electron Eng*, 19(9):1180-1190. https://doi.org/10.1631/FITEE.1601814

Kingni ST, Rajagopal K, Çiçek S, et al., 2020. Dynamic analysis, FPGA implementation, and cryptographic application of an autonomous 5D chaotic system with offset boosting. *Front Inform Technol Electron Eng*, 21(6):950-961. https://doi.org/10.1631/FITEE.1900167

Lai QX, Zhang L, Li ZY, et al., 2009. Analog memory capacitor based on field-configurable ion-doped polymers. *Appl Phys Lett*, 95(21):213503. https://doi.org/10.1063/1.3268433

Li CB, Sprott JC, 2016. Variable-boostable chaotic flows. *Optik*, 127(22):10389-10398. https://doi.org/10.1016/j.ijleo.2016.08.046

Li CB, Thio WJC, Iu HHC, et al., 2018. A memristive chaotic oscillator with increasing amplitude and frequency. *IEEE Access*, 6:12945-12950. https://doi.org/10.1109/ACCESS.2017.2788408

Liu RX, Dong RX, Qin SC, et al., 2020. A new type artificial synapse based on the organic copolymer memcapacitor. *Org Electron*, 81:105680. https://doi.org/10.1016/j.orgel.2020.105680

Ma XJ, Mou J, Liu J, et al., 2020. A novel simple chaotic circuit based on memristor-memcapacitor. *Nonl Dynam*, 100(3):2859-2876. https://doi.org/10.1007/s11071-020-05601-x

Martinez-Rincon J, Pershin YV, 2011. Bistable nonvolatile elastic-membrane memcapacitor exhibiting a chaotic behavior. *IEEE Trans Electron Dev*, 58(6):1809-1812.

https://doi.org/10.1109/TED.2011.2126022

Martinez-Rincon J, di Ventra M, Pershin YV, 2010. Solid-state memcapacitive system with negative and diverging capacitance. *Phys Rev B*, 81(19):195430. https://doi.org/10.1103/PhysRevB.81.195430

Najem JS, Hasan MS, Williams RS, et al., 2019. Dynamical nonlinear memory capacitance in biomimetic membranes. *Nat Commun*, 10:3239. https://doi.org/10.1038/s41467-019-11223-8

Pershin YV, Ventra MD, 2011. Memory effects in complex materials and nanoscale systems. *Adv Phys*, 60(2):145-227. https://doi.org/10.1080/00018732.2010.544961

Pershin YV, Traversa FL, di Ventra M, 2015. Memcomputing with membrane memcapacitive systems. *Nanotechnology*, 26(22):225201. https://doi.org/10.1088/0957-4484/26/22/225201

Pham VT, Akgul A, Volos C, et al., 2017. Dynamics and circuit realization of a no-equilibrium chaotic system with a boostable variable. *AEU-Int J Electron Commun*, 78:134-140. https://doi.org/10.1016/j.aeue.2017.05.034

Pisarchik AN, Feudel U, 2014. Control of multistability. *Phys Rep*, 540(4):167-218. https://doi.org/10.1016/j.physRep2014.02.007

Rajagopal K, Akgul A, Jafari S, et al., 2018a. A chaotic memcapacitor oscillator with two unstable equilibriums and its fractional form with engineering applications. *Nonl Dynam*, 91(2):957-974. https://doi.org/10.1007/s11071-017-3921-3

Rajagopal K, Jafari S, Karthikeyan A, et al., 2018b. Hyperchaotic memcapacitor oscillator with infinite equilibria and coexisting attractors. *Circ Syst Signal Process*, 37(9): 3702-3724. https://doi.org/10.1007/s00034-018-0750-7

Sun JW, Han GY, Wang YF, 2020. Dynamical analysis of memcapacitor chaotic system and its image encryption application. *Int J Contr Autom Syst*, 18(5):1242-1249. https://doi.org/10.1007/s12555-019-0015-7

Wang GY, Cai BZ, Jin PP, et al., 2016. Memcapacitor model and its application in a chaotic oscillator. *Chin Phys B*, 25(1):010503. https://doi.org/10.1088/1674-1056/25/1/010503

Wang GY, Shi CB, Wang XW, et al., 2017a. Coexisting oscillation and extreme multistability for a memcapacitor-based circuit. *Math Probl Eng*, 2017:6504969. https://doi.org/10.1155/2017/6504969

Wang GY, Zang SC, Wang XY, et al., 2017b. Memcapacitor model and its application in chaotic oscillator with memristor. *Chaos*, 27(1):013110. https://doi.org/10.1063/1.4973238

Wang XY, Yu J, Jin CX, et al., 2019. Chaotic oscillator based on memcapacitor and meminductor. *Nonl Dynam*, 96(1): 161-173. https://doi.org/10.1007/s11071-019-04781-5

Wang Z, Akgul A, Pham VT, et al., 2017. Chaos-based application of a novel no-equilibrium chaotic system with coexisting attractors. *Nonl Dynam*, 89(3):1877-1887. https://doi.org/10.1007/s11071-017-3558-2

Wu HG, Ye Y, Bao BC, et al., 2019a. Memristor initial boosting behaviors in a two-memristor-based hyperchaotic system. *Chaos Sol Fract*, 121:178-185. https://doi.org/10.1016/j.chaos.2019.03.005

Wu HG, Ye Y, Chen M, et al., 2019b. Periodically switched memristor initial boosting behaviors in memristive hypogenetic jerk system. *IEEE Access*, 7:145022-145029. https://doi.org/10.1109/ACCESS.2019.2945754

Xu Q, Lin Y, Bao BC, et al., 2016. Multiple attractors in a non-ideal active voltage-controlled memristor based Chua's circuit. *Chaos Sol Fract*, 83:186-200. https://doi.org/10.1016/j.chaos.2015.12.007

Xu Q, Tan X, Zhang YZ, et al., 2020. Riddled attraction basin and multistability in three-element-based memristive circuit. *Complexity*, 2020:4624792. https://doi.org/10.1155/2020/4624792

Yang LB, Yang QG, Chen GR, 2020. Hidden attractors, singularly degenerate heteroclinic orbits, multistability and physical realization of a new 6D hyperchaotic system. *Commun Nonl Sci Numer Simul*, 90:105362. https://doi.org/10.1016/j.cnsns.2020.105362

Yuan F, Li YX, 2019. A chaotic circuit constructed by a memristor, a memcapacitor and a meminductor. *Chaos*, 29(10):101101. https://doi.org/10.1063/1.5125673

Yuan F, Wang GY, Shen YR, et al., 2016. Coexisting attractors in a memcapacitor-based chaotic oscillator. *Nonl Dynam*, 86(1):37-50. https://doi.org/10.1007/s11071-016-2870-6

Yuan F, Deng Y, Li YX, et al., 2019a. The amplitude, frequency and parameter space boosting in a memristor–meminductor-based circuit. *Nonl Dynam*, 96(1):389-405. https://doi.org/10.1007/s11071-019-04795-z

Yuan F, Li YX, Wang GY, et al., 2019b. Complex dynamics in a memcapacitor-based circuit. *Entropy*, 21(2):188. https://doi.org/10.3390/e21020188

Zhang S, Zeng YC, Li ZJ, et al., 2018. Hidden extreme multistability, antimonotonicity and offset boosting control in a novel fractional-order hyperchaotic system without equilibrium. *Int J Bifurc Chaos*, 28(13):1850167. https://doi.org/10.1142/S0218127418501675

Zhang YZ, Liu Z, Wu HG, et al., 2019. Extreme multistability in memristive hyper-jerk system and stability mechanism analysis using dimensionality reduction model. *Eur Phys J Spec Top*, 228(10):1995-2009. https://doi.org/10.1140/epjst/e2019-800238-0

Zhao L, Fan Z, Cheng SL, et al., 2020. An artificial optoelectronic synapse based on a photoelectric memcapacitor. *Adv Electron Mater*, 6(2):1900858. https://doi.org/10.1002/aelm.201900858

Zhou W, Wang GY, Iu HHC, et al., 2020. Complex dynamics of a non-volatile memcapacitor-aided hyperchaotic oscillator. *Nonl Dynam*, 100(4):3937-3957. https://doi.org/10.1007/s11071-020-05722-3

Zhou Z, Yu DS, Wang XY, 2017. Investigation on the dynamic behaviors of the coupled memcapacitor-based circuits. *Chin Phys B*, 26(12):120701. https://doi.org/10.1088/1674-1056/26/12/120701